ChemElectroChem

Research Article
doi.org/10.1002/celc.202300428

Chemistry Europe
European Chemical Societies Publishing

www.chemelectrochem.org

Unlocking High-Performance Supercapacitor Behavior and Sustained Chemical Stability of 2D Metallic $CrSe_2$ by Optimal Electrolyte Selection

Weihao Li,[a] Niklas Wolff,[b] Arun Kumar Samuel,[a] Yuanshen Wang,[a] Vihar P. Georgiev,[c] Lorenz Kienle,[b] and Alexey Y. Ganin*[a]

Supercapacitors are energy storage devices with the ability to rapidly charge and discharge, making them a valuable complement to battery systems. To maximize their fast-charging capabilities, identifying materials and methods to enhance their energy density is crucial. In this work, we carried out a comprehensive study of an emerging 2D dichalcogenide, $CrSe_2$, as a supercapacitor material. We demonstrate that $CrSe_2$ can be obtained at ambient temperature through deintercalation of a relevant $KCrSe_2$ precursor using a 0.5 M solution of I_2 in acetonitrile. Although $CrSe_2$ decomposed in 1 M KOH, it was found to be chemically stable in common electrolytes such as H_2SO_4, Li_2SO_4, and Na_2SO_4. Despite low surface area $CrSe_2$ reached a specific capacitance of 27 $F\,g^{-1}$ in 1 M H_2SO_4 and, thus consistently outperformed high surface carbon black. Computational studies suggested that the metallic conductivity of $CrSe_2$ was likely the primary factor contributing to the superior performance of this 2D chalcogenide over high surface carbon analogues.

Introduction

Supercapacitors (SCs) are devices that store electrical energy by accumulating charge on the surface of electrodes in contact with a polarizable electrolyte. The unique feature of these devices is their ability to charge and discharge rapidly, making them an ideal companion to battery systems. When used together, a SC can act as a buffer for a battery, allowing for a continuous operation even during high-demand situations such as rapid changes in power output during peaks in renewable energy generation.[1]

To fully exploit the potential of SCs with their high-power density and short charge times, it is essential to find ways to increase their energy density. One approach is to increase the surface area of the electrodes, which can help maximize the storage of interface charge.[2] Layered transition metal dichalcogenides (TMDs) provide access to a significant electrode-electrolyte interface, making them ideal targets for utilizing such approach to improving SC performance.[3] Complementary approach is to use electrodes with enhanced conductivity to minimize ohmic losses.[4] In this case, the improved efficiency of the charge and discharge process[5] leads to an overall enhanced performance and a superior SC performance.[6] Several binary TMDs display intrinsic metallic conductivity[7] but only a few of them were studied in SC applications.[8] Recent examples include composites with TiS_2,[9] VS_2,[3,10] and VSe_2.[10,11]

$CrSe_2$ is a metallic conducting selenide[12] which has attracted substantial interest as a tunable 2D magnet.[13] It is commonly referred to as 1T-$CrSe_2$ due to a distinctive crystal structure consisting of edge-sharing octahedra as key building blocks. Despite being an attractive target for SC application, $CrSe_2$ has only been tested one time in 3 M KOH as a part of composite consisting of low crystalline $CrSe_2$ and an MXene (Ti_3C_2).[14] The authors attributed an improved performance of the composite to the strong charge-discharge characteristics of the heterostructure formed between the selenide and MXene. However, since TMDs have been reported to be susceptible to degradation in alkaline aqueous electrolytes,[15] it is unclear whether the actual performance of the hybrid $CrSe_2/Ti_3C_2$ composite has been driven by the TMD or rather by the components used to create the composite. For example, MXenes are excellent materials for SC on their own.[16] Therefore, more careful research is required when novel materials like $CrSe_2$ show improved properties compared with well-studied materials. Preparing $CrSe_2$ as highly crystalline material may provide a better assessment of the SC properties of this 2D selenide as it would allow to account for any potential chemical changes that may happen to this material during the electrochemical process.

[a] W. Li, Dr. A. Kumar Samuel, Y. Wang, Dr. A. Y. Ganin
School of Chemistry
University of Glasgow
Glasgow, G12 8QQ (United Kingdom)
E-mail: Alexey.Ganin@glasgow.ac.uk

[b] Dr. N. Wolff, Prof. L. Kienle
Department of Material Science
Kiel University
Kaiserstrasse 2, 24143 Kiel (Germany)

[c] Prof. V. P. Georgiev
James Watt School of Engineering
University of Glasgow
Glasgow, G12 8QQ (United Kingdom)

Supporting information for this article is available on the WWW under https://doi.org/10.1002/celc.202300428

In this context, previous research has shown that crystalline 1T-$CrSe_2$ can be accessed in bulk quantities by oxidative deintercalation of K from $KCrSe_2$ with I_2 in acetonitrile.[12,17] Both referenced methods seemed to yield crystalline $CrSe_2$ in necessary quantities and thus, the deintercalation process is very well suited for preparing a material that could be used in a systematic evaluation of the (electro)chemical stability of 1T-$CrSe_2$ and its suitability in SC applications.

In this work we demonstrate that the oxidative deintercalation of potassium from $KCrSe_2$ with 0.5 M solution of I_2 in acetonitrile readily yields stoichiometric, polycrystalline 1T-$CrSe_2$ at ambient temperature. However, $CrSe_2$ decomposes readily in 1 M KOH making this chalcogenide unsuitable for SC applications in alkaline media. Still, 1T-$CrSe_2$ remains chemically stable and shows relatively high SC performance (consistent with EDLC behavior) in H_2SO_4, Li_2SO_4 and Na_2SO_4 electrolytes. Furthermore, the addition of 10% graphite allowed us to increase the surface area of the resulting 1T-$CrSe_2$ which led to a significant improvement in SC characteristic of the composite material. Remarkably, both pristine $CrSe_2$ and composite material consistently outperformed high surface area carbon black, reaching the maximum capacitance value of 27 $F\,g^{-1}$ in 1 M H_2SO_4. The superior performance of this 2D chalcogenide over carbon is consistent with our computational work which predicted that the metallic conductivity of $CrSe_2$ was probably the key reason for the improvement.

Results and Discussion

Computational studies on metallic behavior in $CrSe_2$

As mentioned in the introduction the conductivity of the electrode is one of the key factors that governs SC performance. Consequently, we conducted the calculations of the electronic structure of $CrSe_2$. Figure 1 presents the band structure and the Projected Density of States (PDOS) of 1T-$CrSe_2$ as a function of energy, measured in electron volts (eV). As illustrated in Figure 1a, Cr *d*- and Se *p*-orbitals considerably contribute to the band structure, particularly in the vicinity of the Fermi level. Within $CrSe_2$, the Cr *d*-orbitals undergo hybridization with the Se *p*-orbitals, which gives rise to metal-chalcogenide bonding. The Cr *s*-orbitals, being further removed from the Fermi level and less engaged in bonding, have a diminished contribution to the band structure. The PDOS reveals that both Cr *d*- and Se *p*-states contribute to the metallic bonding (Figure 1b). Therefore, $CrSe_2$ demonstrates metallic behavior, characterized by a significant total DOS extending across the Fermi level, indicative of high electronic conductivity. These findings for $CrSe_2$ signal a promising potential for an enhanced conductivity.[10] This is in line with the previous experimental work that demosntrated metallic type of conductivity in $CrSe_2$.[12]

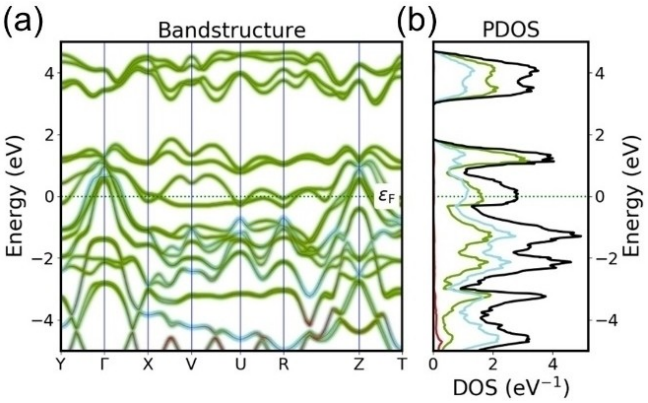

Figure 1. Calculated electronic structure of 1T-$CrSe_2$. (a) Projected band structures (Red: Cr *s*-orbitals, Green: Cr *d*-orbitals and Blue: Se *p*-orbitals) and (b) Density of states of $CrSe_2$. (Red: Cr *s*-orbitals, Green: Cr *d*-orbitals, Blue: Se *p*-orbitals and black: total DOS). The dashed line situated at 0 eV represents the Fermi Level.

Synthesis and characterization of $KCrSe_2$ precursors

In line with the previous literature reports (see crystal structure in Figure 2a) $KCrSe_2$ readily forms from the elements upon reaction inside a sealed ampoule.[12b,17] We used a lower temperature of 600 °C than previously reported[17] because it allowed us to employ Pyrex ampoules. These are substantially cheaper and easier to seal than quartz ampoules. In addition, as no significant reaction with the Pyrex ampoules was noticed we opted out for Pyrex inserts instead of alumina crucibles. After additional annealing to ensure the homogeneity of the product the resulting PXRD pattern (Figure 2b) was found to be consistent with a simulated pattern.[17] Furthermore, the LeBail refinement of the PXRD data (Figure S1) against the reported crystal structure (Figure 2a, Space group: *C*2/*m*) of $KCrSe_2$ revealed that the unit cell parameters ($a = 6.5720(9)$ Å, $b = 3.7938(2)$ Å, $c = 7.6580(1)$, $\beta = 106.68(3)°$) were comparable with those reported by Schoop's group ($a = 6.5845$ Å, $b = 3.8012$ Å, $c = 7.7116$ Å, $\beta = 106.548°$). This suggested that the simplifica-

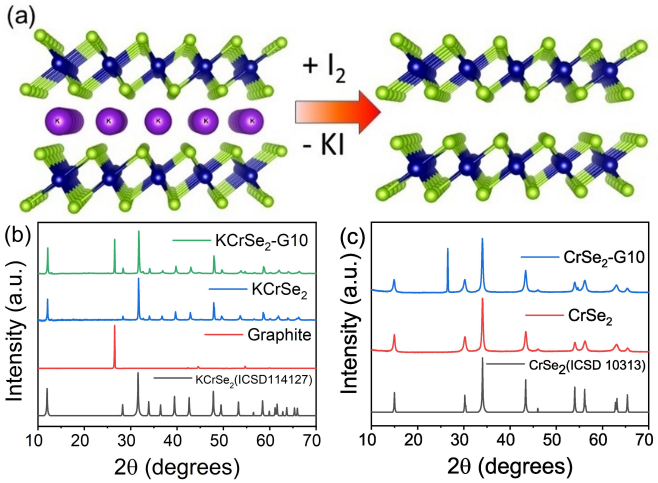

Figure 2. (a) Crystal structure of the layered $KCrSe_2$ and $CrSe_2$ with the schematic illustration of the deintercalation process (Navy: Cr, Green: Se and purple: K). (b) PXRD patterns of $KCrSe_2$-G10 (green), $KCrSe_2$ (blue), graphite (red), and simulated $KCrSe_2$ (black). The background was subtracted for a better comparison. (c) PXRD patterns of $CrSe_2$-G10 (blue), $CrSe_2$ (red), and simulated $CrSe_2$ (black).

tion of the experimental procedure had no detrimental impact on the purity of the $KCrSe_2$ product. We should note that we opted out for LeBail refinement of the data instead of Rietveld due to a strong X-ray absorption (Total $\mu R = 15.68$) from $KCrSe_2$ when it is measured in a capillary in a Debye-Scherrer geometry.

The same reaction protocol (except 10 wt. % of graphite was added) yielded a $KCrSe_2$ product (denoted as $KCrSe_2$-G10) which along with the peaks matching $KCrSe_2$ simulated pattern showed some small additional peaks (Figure 2b). The LeBail refinement of the experimental data (Figure S2) against a structural model showed that the experimental unit cell parameters $a = 6.5631(1)$ Å, $b = 3.7909(1)$ Å, $c = 7.6365(1)$ Å and $\beta = 106.786°$ for $KCrSe_2$ and $a = 2.4578(4)$ Å and $c = 6.71326(2)$ Å for graphite were consistent with the previously reported data. We could not assign unfitted peaks, but they probably originate from a potassium deficient $K_{1-x}CrSe_2$ phase ($x < 1$). However, as revealed in the following section the presence of this impurity had no detrimental effect on $CrSe_2$ product. Therefore, we did not pursue the optimization process that would allow us to eliminate the K-deficient phase completely.

Synthesis and characterization of $CrSe_2$ by the deintercalation of $KCrSe_2$

In line with the previous report,[17] the oxidative deintercalation of potassium (Figure 2a) proceeds readily from $KCrSe_2$ and $KCrSe_2$-G10 in acetonitrile. It should be noted that for the deintercalation we employed 0.5 M I_2/acetonitrile solution (instead of previously reported 0.01 M).[17] Despite using the concentrated solution both samples (denoted as $CrSe_2$ and $CrSe_2$-G10 respectively) displayed experimental PXRD patterns which were consistent with the simulated pattern of the hexagonal 1T-$CrSe_2$ (Figure 2c). LeBail refinement of the experimental profile (Figure S3, S4) against a reported crystal structure of $CrSe_2$ (Figure 2a, Space group: *P*-3 *m*1) also revealed the units cell parameters ($a = 3.3898(3)$ Å and $c = 5.9099(4)$ Å on $CrSe_2$) and ($a = 3.3910(3)$ Å and $c = 5.9144(3)$ Å on $CrSe_2$-G10) that were practically identical to previously reported ($a =$ 3.3908 Å and $c = 5.9136$ Å).[17] The additional peaks originated solely from graphite and gave the unit cell parameters ($a =$ 2.458(3) and $c = 6.700(3)$ Å) which were again consistent with the expected values. The comparison of the unit cell parameters for the $CrSe_2$ samples with the literature is given in the Table S1.

The representative EDX spectrum of $CrSe_2$ is shown in Figure S5. The respective peaks for Cr, Se as well as K traces are well resolved, making Cr:Se ratio determined by EDX reliable. The evaluation across of at least 5 different spots returned the Se:Cr ratio of 2.01 ± 0.1 for $CrSe_2$ and Se:Cr $= 2.04 \pm 0.1$ for $CrSe_2$-G10. Both values are consistent with the expected stoichiometry within the standard deviations. The traces of 0.67 ± 0.09 at. % K were detected in $CrSe_2$ samples, and $0.71 \pm$ 0.2 at.% K in $CrSe_2$-G10. This was inevitable (due to the nature of the deintercalation process) with some K remained adsorbed on the surface despite rigorous washing.

The results of the X-ray photoelectron spectroscopy (XPS) displayed in Figure S6 and S7 were consistent with the composition detected by EDXS. The spectra (confirming the oxidation states of Cr and Se; BE Cr 2p3/2 588.4 eV and Se 3d5/ 2 59.35 eV) were in line with the expectation based on literature.[13,18] In addition, BE of Cr peaks are expectedly shifted up the BE in comparison with the Cr_2Se_3 spectra confirming the oxidation state $+4$.[19]

Assessment of the scanning electron microscopy (SEM) images (Figure S8) revealed that $CrSe_2$ and $CrSe_2$-G10 samples showed similar morphologies. They consisted of thin, well-dispersed, micrometre-scale platelets with approximate dimensions within 1–10 μm range. The large particle sizes observed in SEM images contradict the results of PXRD. In the PXRD patterns (Figure 2b) the reflections are broadened quite significantly which suggested that the lateral particle sizes were small. However, the discrepancy is probably due to the deintercalation process which leads to a misalignment of the plates resulting in a significant broadening of the reflections.[20] Additional elemental mapping of $CrSe_2$-G10 suggested that the graphite particles are randomly dispersed within $CrSe_2$ matrix without any morphological order (Figure S9–S11). As evident from Figure S11 the size of the graphite particles within $CrSe_2$ matrix ranges between 1–10 μm. In comparison an SEM image (Figure S12) collected on the original graphite sample shows that the particle sizes are larger than those of graphite particles in $CrSe_2$-G10. This suggests that the size of graphite particles changes during the intercalation process.

In depth transmission electron microscopy (TEM) on $CrSe_2$ sample as exemplified in Figure 3a showed that the sample consisted of thin, plate-like microscale crystals rather than nanoparticles (as one had expected given significant broadening of the PXRD peaks). Selected-area electron diffraction (SAED) experiments were conducted on thin crystalline areas as shown in Figure 3b which were referenced to the [001] crystal orientation of $CrSe_2$. Since the crystalline areas rapidly turned amorphous under the focused scanning electron beam, we switched to the high resolution (HRTEM) imaging mode for the local structure investigation as presented in Figure 3c. Here, single crystalline regions showing the [001] lattice motif were identified (compare Fast Fourier Transforms (FFT) with SAED pattern in Figure S13). With regards to probable peak broadening in PXRD patterns, also secondary orientations of the $CrSe_2$ phase and slight variance of in-plane lattice spacings were observed in both SAED and HRTEM + FFT analysis demonstrating a considerable structural disorder between crystal sheets. (Figure S14). Further, the spatial distribution of Cr and Se elements presented in the EDXS maps of Figure 3d-f returned the Se:Cr ratio of 2.07 ± 0.02 which is consistent with the results of EDX analysis recorded on the bulk sample. In addition, the quantification result of EDXS maps for the total recorded EDX spectra (Figure S15) also returned 0.9 at.% of K. Although the TEM results suggested that on average the sample can be viewed as fully K-deintercalated $CrSe_2$ product, it should be noted that local regions with significantly higher K composition and grain morphology (content up to 11 at.%) were identified as possible side products of the deintercalation process. This is

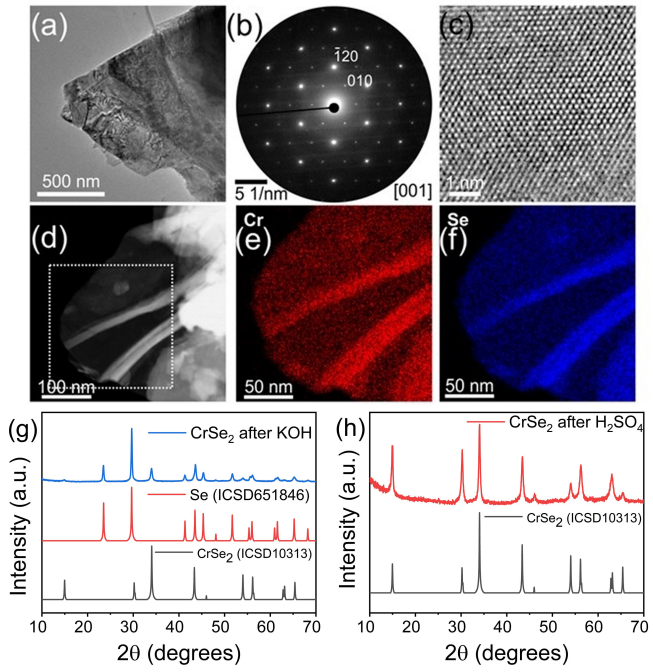

Figure 3. TEM investigation of $CrSe_2$. (a) TEM image of a $CrSe_2$ crystal and (b) corresponding electron diffraction pattern showing the [001] crystal orientation of the trigonal (*P*-3 *m*1) $CrSe_2$ phase. (c) HRTEM micrograph of a thin region. (d-f) STEM image and EDXS maps showing the elemental distribution of Cr = red and Se = blue within the framed region. (g,h) PXRD patterns of $CrSe_2$ before and after 24 hrs stirring in 1 M KOH and in 1 M H_2SO_4.

consistent with the previous work where the authors noticed the similar phenomenon.[17]

Raman spectroscopy on $CrSe_2$ revealed that a relatively strong peak was present at *ca.* 232 cm^{-1} (Figure S16). As the sample was highly beam sensitive it was not possible to accumulate sufficient signal for a high-quality data resulting in a slight difference in peak positions due to high background. Still, the spectra were of sufficient quality to attribute the peak position to the predicted and experimental $CrSe_2$ spectra with the recorded peak ascribed to the A_1 mode. The peak position associated with this mode was predicted to appear at 230 cm^{-1} and was confirmed experimentally at 258 cm^{-1}.[13,21] It should be noted that Raman signal at approximately 545 cm^{-1} has been reported as the one originating from $CrSe_2$.[14] However, as evident from Figure S17 this peak tends to appear and then keeps increasing upon prolonged exposure of the sample to the beam. The prolonged exposure can be visually tracked from optical images as a distinctive "beam burn" spot emerges and grows with the exposure time (Figure S18). Similarly, the Raman spectrum of $CrSe_2$-G10 demonstrated the presence of the A_1 vibration mode at approximately 251 cm^{-1} (Figure S19) consistent with the expected 1T-$CrSe_2$ phase. Additional Raman peaks located at approximately 1343 cm^{-1}, 1580 cm^{-1}, 2452 cm^{-1}, and 2718 cm^{-1} confirmed the presence of graphite. The absence of any additional peaks implied that there was no chemical bond between $CrSe_2$ and graphite in the sample. Overall, the characterization methods provided sufficient evidence that the synthesized samples were consistent with the targeted $CrSe_2$ composition making them reliable samples for chemical and electrochemical investigation. After comprehensive studies under controlled laser power conditions and in an inert atmosphere, we concluded that the peak at ca. 545 cm^{-1} in the Raman spectra of $CrSe_2$ is due to beam decomposition. The actual peak for $CrSe_2$ is located at *ca.* 250 cm^{-1} consistent with the theoretical calculations for A_{1g} mode.

Chemical and electrochemical properties of $CrSe_2$

Before investigating the electrochemical behavior of $CrSe_2$, its chemical stability was assessed in various aqueous media to identify an optimal electrolyte. The stability of $CrSe_2$ was initially examined by stirring the samples in H_2O for 24 hours, with the subsequent PXRD analysis (Figure S20) confirming $CrSe_2$ was stable in water. However, we found $CrSe_2$ completely unstable in a 1 M KOH aqueous solution because after 24 hours of stirring, the PXRD pattern of the resulting product (Figure 3g) showed strong peaks corresponding to the Se simulated pattern. Similar diffraction patterns were observed after stirring $CrSe_2$ powders in 1 M LiOH and NaOH solutions (Figure S21 and S22). Consequently, alkaline environments were deemed unsuitable for subsequent electrochemical tests. This casts some doubt whether the previously reported supercapacitive behavior in MXene/$CrSe_2$ in 3 M KOH is originated from $CrSe_2$.[14]

In contrast, after $CrSe_2$ was stirred in a 1 M H_2SO_4 solution for 24 hours, it showed a PXRD pattern (Figure 3h) which was in a good agreement with the simulated $CrSe_2$ pattern. The samples were stable in a 1 M Na_2SO_4 solution as well (Figure S23).

The cyclic voltammetry (CV) profiles of products (immobilized as inks on Ti foils and tested in in 1 M H_2SO_4 at 50 mV s^{-1}) are shown in Figure 4a. A continuous symmetrical shape without any additional peaks of the CV profiles is consistent with the electric double-layer capacitance (EDLC) behavior. This is further confirmed by the analysis of the shape of the CV curves measured at different sweep rates (Figure S24). The galvanostatic charge-discharge (GCD) experiments were conducted to examine the behavior and specific capacitance under current density of 1 and 2 A g^{-1} (Figure 4b and S21). In line with the CV data, the distinctive triangular shape of GCD profiles indicates the EDLC behavior. The abrupt decrease in current values at the onset of discharging can be attributed to the material's internal resistance The calculation of the specific capacitance (see Suppl. Note 1) gave the values of 1.2 F g^{-1} for graphite, 3.7 F g^{-1} for $CrSe_2$ and 27.3 F g^{-1} for $CrSe_2$-G10 at 1 A g^{-1}. The difference between graphite and $CrSe_2$ is expectable due to the superior conductivity of 1T-$CrSe_2$ phase as discussed above. However, as the size of the particles in $CrSe_2$ and $CrSe_2$-G10 according to SEM were quite similar, the drastic difference in electrochemical performance between two samples, also at higher current rates (Figure S25), is surprising.

To account for this difference in performance we measured surface area of the samples by nitrogen gas adsorption. However, the measurements on pristine $CrSe_2$ were unsuccessful as evidenced by the decoupling of adsorption/desorption

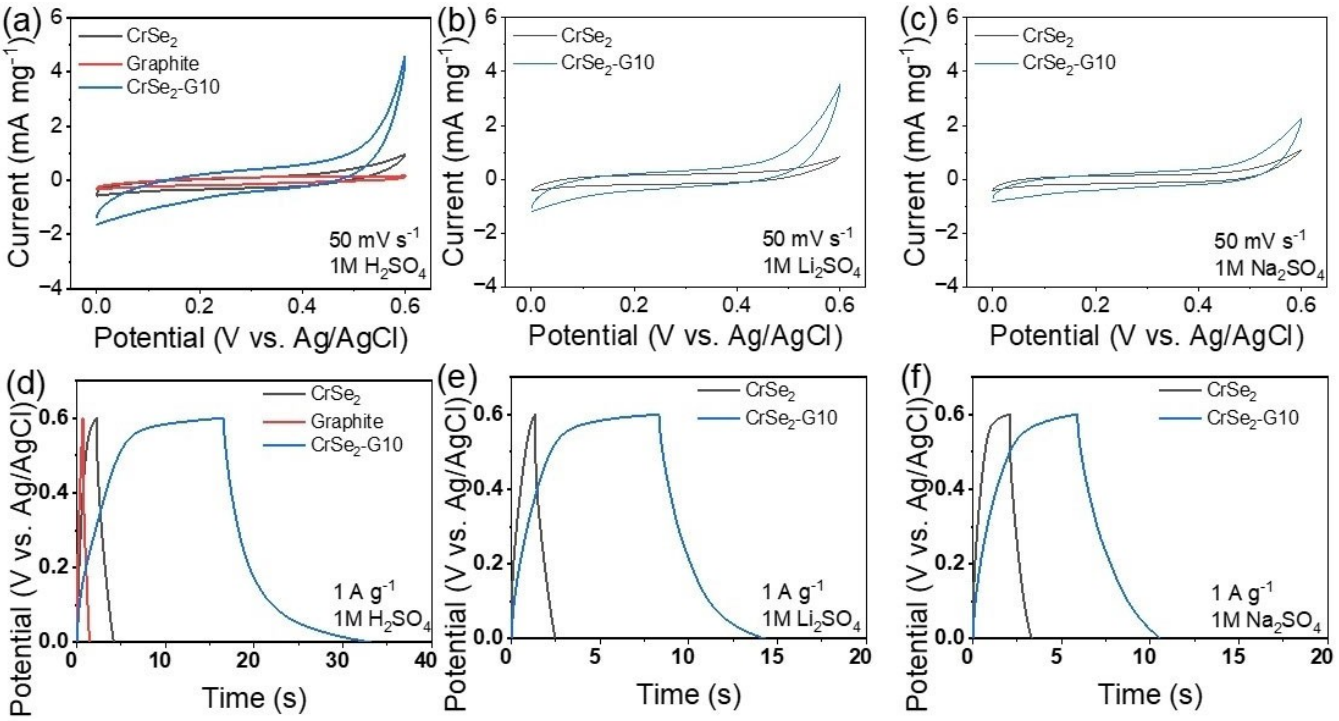

Figure 4. CV profiles of $CrSe_2$, graphite, and $CrSe_2$-G10 at 50 mV s^{-1} in (a) 1 M H_2SO_4; (b) 1 M Li_2SO_4 and (c) 1 M Na_2SO_4. GCD profiles of $CrSe_2$, graphite, and $CrSe_2$-G10 at 1 A g^{-1} in (d) 1 M H_2SO_4; (e) 1 M Li_2SO_4 and (f) 1 M Na_2SO_4.

isotherms (Figure S26) which suggested that the specific surface area of the sample was $<2\ m^2 g^{-1}$. However, $CrSe_2$-G10 displayed well-defined N_2-adsorption/desorption isotherms (Figure S27) which led to a significantly improved Brunauer-Emmett-Teller (BET) surface area of 7.63 $m^2 g^{-1}$. In addition, the Type H3 hysteresis loop is consistent with the material containing aggregates of plate-like particles.[22] Similar gas-sorption results were revealed for graphite (BET surface area 6.89 $m^2 g^{-1}$) (Figure S28). Overall, adding 10 wt.% of graphite during the initial synthesis of $KCrSe_2$ sample leads to reduction in graphite particle sizes (as discussed above in the SEM section) and possibly helps to create an open network architecture resulting in an improved performance.

In addition to sulfuric acid other chemically benign electrolytes have been considered. When 1 M Li_2SO_4 was used as an electrolyte all three samples demonstrated CV loops which were consistent with the EDLC behavior (Figure 4c). Similar type of the behavior was revealed at different sweep rates (Figure S29). The GCD profiles also confirmed the EDLC type behavior (Figure 4d and Figure S30). $CrSe_2$-G10 showed the specific capacitance of 9.9 F g^{-1} while the capacitance of $CrSe_2$ was 0.56 F g^{-1}. $CrSe_2$ was also tested in 1 M Na_2SO_4 whereby the CV curves and GCD profiles (Figure 4 and Figure S31-32) indicated EDLC behavior. The resulting values of the specific capacitance were 0.7 F g^{-1} ($CrSe_2$) and 7.7 F g^{-1} ($CrSe_2$-G10). In addition, as shown in Figure S33 both materials retained well the capacity after 700 cycles. The comparison of the recorded values of samples in H_2SO_4, Li_2SO_4 and Na_2SO_4 electrolytes is given in the Table S2.

There is little literature data on the electrochemical stability of the products after supercapacitors tests. However, we noticed that all $CrSe_2$ samples tested remained intact after electrochemical investigation, with no phase changes or decomposition observed, as confirmed by PXRD (Figure S34). These findings are consistent with the chemical stability tests, demonstrating that $CrSe_2$ is stable in H_2SO_4, Li_2SO_4, and Na_2SO_4 solutions. Similarly, the high magnification SEM images (Figure S35) on $CrSe_2$-G10 sample before and after testing in H_2SO_4 point out that the morphology of the sample remains unchanged.

Finally, to add an additional benchmark we carried out electrochemical measurements on carbon black sample with the BET surface area of 65.2 $m^2 g^{-1}$ according to adsorption-desorption N_2 isotherm measurements (Figure S36). Notably, $CrSe_2$-G10 outperformed this high surface area carbon black in all electrolytes by a large margin despite having the surface area of 10 times lower (Figure S37 and S38). Furthermore, the specific capacitance of $CrSe_2$ was higher than some other 2D chalcogenides (Table S3), for example, in Na_2SO_4 electrolyte the reported values on $MoSe_2$ 2.6 F g^{-1} or WS_2 3.5 F g^{-1} are somewhat lower despite appreciably high surface areas.[23] However, there is still a room for improvement as $CrSe_2$ does not outperform a range of other

TMD materials immobilized on high surface area substrates. This is expectable given that the specific surface area of all tested $CrSe_2$ samples were below $<10\ m^2 g^{-1}$. This clearly suggests that the effective strategies for a better SC performance is to increase the surface area in this TMD.

Conclusions

In conclusion, high-quality, stoichiometric, polycrystalline $CrSe_2$ can be synthesized using the deintercalation method. In line with our electronic structure calculations, $CrSe_2$ demonstrates metallic conductivity, making it a good candidate for supercapacitor applications. From the electrochemical measurements in a three-electrode system, EDLC behavior is evident from cycling voltammetry, suggesting that improving surface area is key to improving performance. However, the metallic conductivity in $CrSe_2$ makes it a superior electrode material to a significantly higher surface area carbon black electrode. This creates opportunities for future implementation of this emerging 2D material if it can be synthesized as a high surface area product. This is evident for the $CrSe_2$-G10 sample, in which a marginal increase of surface area to $7.63\ m^2 g^{-1}$ led to specific capacitance of $27.3\ F g^{-1}$ in 1 M H_2SO_4 at $1\ A g^{-1}$. This again reinforces the notion that the access to a sufficiently high surface area $CrSe_2$ product would enable access to a high performance SC material.

Supporting Information

The supporting information contains LeBail refinement $KCrSe_2$, $KCrSe_2$-G10, $CrSe_2$ and $CrSe_2$-G10. Additional SEM-DEX and mapping for $CrSe_2$ and $CrSe_2$-G10. XRD and Raman spectroscopy plots and TEM for $CrSe_2$. Related electrochemical test and after electrochemical characterization for $CrSe_2$ and $CrSe_2$-G10 are included as well. The authors have cited additional references within the Supporting Information.[10b,12b,14,17,23–31]

Acknowledgements

A.Y.G. and A.K.S. acknowledge the EPSRC (EP/W03333X/1) for supporting this work. N.W. and L.K. acknowledge the financial support by German Research Foundation (DFG) under the scheme of the collaborative research centre (CRC)1261/286471992. W.L. thanks China Scholarship Council for providing him with the scholarship.

Conflict of Interests

The authors declare no conflict of interest.

Data Availability Statement

The data that support the findings of this study are available from the corresponding author upon reasonable request.

Keywords: supercapacitors · 2D materials · chromium · solid-state reactions · electric double-layer capacitance

[1] a) Q. Zeng, Y. Lai, L. Jiang, F. Liu, X. Hao, L. Wang, M. A. Green, *Adv. Energy Mater.* **2020**, *10*, 1903930; b) D. P. Chatterjee, A. K. Nandi, *J. Mater. Chem. A* **2021**, *9*, 15880–15918.
[2] M. Atwa, X. Li, D. O'Connell, R. Sui, R. Marriott, V. Birss, *Chem. Mater.* **2023**, *35*, 395–404.
[3] a) J. V. Vaghasiya, C. C. Mayorga-Martinez, J. Vyskočil, Z. Sofer, M. Pumera, *Adv. Funct. Mater.* **2020**, *30*, 2003673; b) A. Khalil, Q. Liu, Q. He, T. Xiang, D. Liu, C. Wang, Q. Fang, L. Song, *RSC Adv.* **2016**, *6*, 48788–48791; c) M. Xia, J. Ning, D. Wang, X. Feng, B. Wang, H. Guo, J. Zhang, Y. Hao, *Chem. Eng. J.* **2021**, *405*, 126611; d) S. Hussain, D. Vikraman, M. T. Mehran, M. Hussain, G. Nazir, S. A. Patil, H.-S. Kim, J. Jung, *Renewable Energy* **2022**, *185*, 585–597; e) Z. Guo, L. Yang, W. Wang, L. Cao, B. Dong, *J. Mater. Chem. A* **2018**, *6*, 14681–14688; f) W. Xiao, Q. He, Y. Zhao, *Appl. Surf. Sci.* **2021**, *570*, 151213.
[4] a) Z.-Z. Chen, J. Hou, J. Zhou, P. Huang, H. Wang, C. Xu, *Rare Met.* **2021**, *40*, 3185–3194; b) G. Zhang, X. Li, D. Wei, H. Yu, J. Ye, S. Chen, W. Zhang, J. Zhu, X. Duan, *Chem. Eng. J.* **2023**, *453*, 139841; c) Y. Sun, E. Sviridova, M. Kamp, J. Zhang, L. Kienle, D. A. J. Moran, O. Guselnikova, A. Y. Ganin, *ACS Appl. Energ. Mater.* **2023**, *6*, 1265–1273.
[5] J. C. McGlynn, M. Friskey, A. Y. Ganin, *Sustain. Energy Fuels* **2020**, *4*, 4473–4477.
[6] Q. Li, H. Wang, X. Tang, M. Zhou, H. Zhao, Y. Xu, W. Xiao, Y. Lei, *Adv. Funct. Mater.* **2021**, *31*, 2101081.
[7] A. Y. Ganin, M. D. Symes, *Curr. Opin. Electrochem.* **2022**, *34*, 101001.
[8] a) Z. Jiang, Y. Wang, S. Yuan, L. Shi, N. Wang, J. Xiong, W. Lai, X. Wang, F. Kang, W. Lin, C. P. Wong, C. Yang, *Adv. Funct. Mater.* **2019**, *29*, 1807116; b) G. H. Han, D. L. Duong, D. H. Keum, S. J. Yun, Y. H. Lee, *Chem. Rev.* **2018**, *118*, 6297–6336; c) W. Xu, Y. Ke, Z. Wang, W. Zhang, A. T. S. Wee, *Surf. Sci. Rep.* **2021**, *76*, 100542.
[9] a) X. Zang, C. Shen, E. Kao, R. Warren, R. Zhang, K. S. Teh, J. Zhong, M. Wei, B. Li, Y. Chu, M. Sanghadasa, A. Schwartzberg, L. Lin, *Adv. Mater.* **2018**, *30*, 1704754; b) G. A. Muller, J. B. Cook, H.-S. Kim, S. H. Tolbert, B. Dunn, *Nano Lett.* **2015**, *15*, 1911–1917.
[10] a) A. Sharma, C. S. Rout, *Int. J. Energy Res.* **2022**, *46*, 24537–24553; b) J. Feng, X. Sun, C. Wu, L. Peng, C. Lin, S. Hu, J. Yang, Y. Xie, *J. Am. Chem. Soc.* **2011**, *133*, 17832–17838.
[11] a) K. A. S. Raj, C. S. Rout, *Emergent Mater.* **2021**, *4*, 1037–1046; b) K. A. Sree Raj, A. S. Shajahan, B. Chakraborty, C. S. Rout, *Chem. Eur. J.* **2020**, *26*, 6662–6669; c) C. Wang, X. Wu, H. Xu, Y. Zhu, F. Liang, C. Luo, Y. Xia, X. Xie, J. Zhang, C. Duan, *Appl. Phys. Lett.* **2019**, *114*, 023902.
[12] a) G. A. Wiegers, *Physica B+C* **1980**, *99*, 151–165; b) C. F. van Bruggen, R. J. Haange, G. A. Wiegers, D. K. G. de Boer, *Physica B+C* **1980**, *99*, 166–172.
[13] B. Li, Z. Wan, C. Wang, P. Chen, B. Huang, X. Cheng, Q. Qian, J. Li, Z. Zhang, G. Sun, B. Zhao, H. Ma, R. Wu, Z. Wei, Y. Liu, L. Liao, Y. Ye, Y. Huang, X. Xu, X. Duan, W. Ji, X. Duan, *Nat. Mater.* **2021**, *20*, 818–825.
[14] K. A. S. Raj, N. Barman, N. K. R. Thapa, C. S. Rout, *Sustain. Energy Fuels* **2022**, *6*, 5187–5198.
[15] V. Shukla, A. Stone, M. McGrath, A. Kane, R. Hurt, *Environ. Sci.-Nano* **2022**, *9*, 2297–2319.
[16] a) R. B. Rakhi, B. Ahmed, M. N. Hedhili, D. H. Anjum, H. N. Alshareef, *Chem. Mater.* **2015**, *27*, 5314–5323; b) M. Zhang, L. He, T. Shi, R. Zha, *Chem. Mater.* **2018**, *30*, 7391–7412.
[17] X. Song, S. N. Schneider, G. Cheng, J. F. Khoury, M. Jovanovic, N. Yao, L. M. Schoop, *Chem. Mater.* **2021**, *33*, 8070–8078.
[18] X. Song, G. Cheng, D. Weber, F. Pielnhofer, S. Lei, S. Klemenz, Y.-W. Yeh, K. A. Filsinger, C. B. Arnold, N. Yao, L. M. Schoop, *J. Am. Chem. Soc.* **2019**, *141*, 15634–15640.
[19] X. Zhu, H. Liu, L. Liu, L. Ren, W. Li, L. Fang, X. Chen, L. Xie, Y. Jing, J. Chen, S. Liu, F. Ouyang, Y. Zhou, X. Xiong, *Chem. Mater.* **2021**, *33*, 3851–3858.
[20] A. Y. Ganin, L. Kienle, G. V. Vajenine, *J. Solid State Chem.* **2006**, *179*, 2339–2348.
[21] D. Çakır, F. M. Peeters, C. Sevik, *Appl. Phys. Lett.* **2014**, *104*, 203110.

[22] M. Thommes, K. Kaneko, A. V. Neimark, J. P. Olivier, F. Rodriguez-Reinoso, J. Rouquerol, K. S. W. Sing, *Pure Appl. Chem.* **2015**, *87*, 1051–1069.
[23] M. A. Bissett, S. D. Worrall, I. A. Kinloch, R. A. W. Dryfe, *Electrochim. Acta* **2016**, *201*, 30–37.
[24] B. H. Toby, R. B. Von Dreele, *J. Appl. Crystallogr.* **2013**, *46*, 544–549.
[25] C. Fang, C. Van Bruggen, R. De Groot, G. Wiegers, C. J. J. o. P. C. M. Haas, *J. Phys. Condens. Matter* **1997**, *9*, 10173.
[26] J. P. Perdew, K. Burke, M. Ernzerhof, *Phys. Rev. Lett.* **1996**, *77*, 3865–3868.
[27] C. Wang, X. Wu, Y. Ma, G. Mu, Y. Li, C. Luo, H. Xu, Y. Zhang, J. Yang, X. Tang, J. Zhang, W. Bao, C. Duan, *J. Mater. Chem. A* **2018**, *6*, 8299–8306.
[28] K. Krishnamoorthy, G. K. Veerasubramani, P. Pazhamalai, S. J. Kim, *Electrochim. Acta* **2016**, *190*, 305–312.
[29] S. K. Balasingam, J. S. Lee, Y. Jun, *Dalton Trans.* **2015**, *44*, 15491–15498.
[30] K. Sambath Kumar, N. Choudhary, D. Pandey, Y. Ding, L. Hurtado, H.-S. Chung, L. Tetard, Y. Jung, J. Thomas, *J. Mater. Chem. A* **2020**, *8*, 12699–12704.
[31] P. Iamprasertkun, W. Hirunpinyopas, V. Deerattrakul, M. Sawangphruk, C. Nualchimplee, *Nanoscale Adv.* **2021**, *3*, 653–660.

Manuscript received: August 28, 2023
Revised manuscript received: September 12, 2023
Version of record online: September 29, 2023